Experimental

A series of aqueous colloidal CdTe solutions were prepared by adding freshly prepared NaHTe solution to N_2-saturated $CdCl_2$ solutions at pH 9.0 in the presence of thiols as stabilizing agents [6]. Two different precursor concentrations were used in this approach, [Cd] = 0.00125 N and [Cd] = 0.0188 N. The molar ratio of Cd^{2+}/thiols/HTe^- was fixed at 1:2.4:0.2. 40 mL CdTe precursor was put into a Teflon-lined stainless steel autoclave with a volume of 50 mL. The autoclaves were maintained at the desired growth temperature (160 and 180 °C). Each autoclave was cooled to room temperature at regular time intervals after the initial heating. To obtain the sample's growth at 100 °C, CdTe precursors were refluxed under open-air conditions [6], aliquots of the crude solutions were taken at different stages of particle growth. No post-preparative treatment was performed on any of the samples for optical characterization. The PL QYs of differently sized CdTe nanocrystals were estimated at room temperature using quinine in aqueous 0.5 N H_2SO_4 as PL reference [7].

Nanocrystal labeled mouse L929 cells were prepared by two separate steps. First, 3-mercaptopropionic acid-stabilized CdTe nanocrystals were conjugated with interferon by sulfo-NHS (*N*-hydroxysulfosuccinimide sodium salt) at pH 9.0. The carboxylic acid group of 3-mercaptopropionic acid-stabilized CdTe can form amide bonds with the primary amine groups of the interferon. Next, the nanocrystal conjugated interferon binds with the receptor on the surface of the mouse cells [16]. Thus, CdTe nanocrystals with different PL emission were labeled on the plasmic membrane of living cells. Thiolglycolic acid-stabilized CdTe nanocrystals are bound to avidin by a similar method as mentioned above, and then by ligand–receptor binding.

Ultraviolet-visible (UV-vis) absorption spectra were obtained using a Shimadzu 3100 UV-vis-near-infrared spectrophotometer. Fluorescence experiments were performed using a Shimadzu RF-5301 PC spectrofluorimeter. All optical measurements were performed at room temperature under ambient conditions. TEM images and SAED were recorded on a JEOL-2010 electron microscope operating at 200 kV. XRD was carried out using a Siemens D5005 diffractometer. An Olympus DX-60 fluorescence microscope was used to examine the nanocrystal labeled cells.

Received: July 6, 2003
Final version: July 28, 2003

[1] a) M. Bruchez Jr., M. Moronne, P. Gin, S. Weiss, A. P. Alivisatos, *Science* **1998**, *281*, 2013. b) W. C. W. Chan, S. Nie, *Science* **1998**, *281*, 2016. c) B. Dubertret, P. Skourides, D. J. Norris, V. Noireaux, A. H. Brivanlou, A. Libchaber, *Science* **2002**, *298*, 1759. d) D. R. Larson, W. R. Zipfel, R. M. Williams, S. W. Clark, M. P. Bruchez, F. W. Wise, W. W. Webb, *Science* **2003**, *300*, 1434. e) H. Mattoussi, J. M. Mauro, E. R. Goldman, G. P. Anderson, V. C. Sundar, F. V. Mikulec, M. G. Bawendi, *J. Am. Chem. Soc.* **2000**, *122*, 12 142. f) D. Gerion, W. J. Parak, S. C. Williams, D. Zanchet, C. M. Micheel, A. P. Alivisatos, *J. Am. Chem. Soc.* **2002**, *124*, 7070. g) A. Schroedter, H. Weller, R. Eritja, W. E. Ford, J. M. Wessels, *Nano Lett.* **2002**, *2*, 1363. h) S. Wang, N. Mamedova, N. A. Kotov, W. Chen, J. Studer, *Nano Lett.* **2002**, *2*, 817. i) D. Wang, A. L. Rogach, F. Caruso, *Nano Lett.* **2002**, *2*, 857.

[2] a) M. Han, X. Gao, J. Z. Su, S. Nie, *Nat. Biotechnol.* **2001**, *19*, 631. b) M. Trau, B. J. Battersby, *Adv. Mater.* **2001**, *13*, 975. c) N. Gaponik, I. L. Radtchenko, G. B. Sukhorukov, H. Weller, A. L. Rogach, *Adv. Mater.* **2002**, *14*, 879. d) Y. Chen, Z. Rosenzweig, *Nano Lett.* **2002**, *2*, 1299.

[3] N. Gaponik, D. V. Talapin, A. L. Rogach, K. Hoppe, E. V. Shevchenko, A. Kornowski, A. Eychmüller, H. Weller, *J. Phys. Chem. B* **2002**, *106*, 7177.

[4] a) D. G. Kurth, P. Lehmann, C. Lesser, *Chem. Commun.* **2000**, 949. b) M. Y. Gao, J. Sun, E. Dulkeith, N. Gaponik, U. Lemmer, J. Feldmann, *Langmuir* **2002**, *18*, 4098.

[5] M. Y. Gao, S. Kirstein, H. Möhwald, A. L. Rogach, A. Kornowski, A. Eychmüller, H. Weller, *J. Phys. Chem. B* **1998**, *102*, 8360.

[6] a) H. Zhang, Z. Zhou, B. Yang, M. Y. Gao, *J. Phys. Chem. B* **2003**, *107*, 8. b) H. Zhang, Z. Cui, Y. Wang, K. Zhang, X. Ji, C. Lü, B. Yang, M. Y. Gao, *Adv. Mater.* **2003**, *15*, 777.

[7] D. V. Talapin, A. L. Rogach, E. V. Shevchenko, A. Kornowski, M. Haase, H. Weller, *J. Am. Chem. Soc.* **2002**, *124*, 5782.

[8] a) C. B. Murray, D. J. Norris, M. G. Bawendi, *J. Am. Chem. Soc.* **1993**, *115*, 8706. b) W. W. Yu, X. Peng, *Angew. Chem. Int. Ed.* **2002**, *41*, 2368.

[9] a) L. Qu, Z. A. Peng, X. Peng, *Nano Lett.* **2001**, *1*, 333. b) A. L. Rogach, D. V. Talapin, E. V. Shevchenko, A. Kornowski, M. Haase, H. Weller, *Adv. Funct. Mater.* **2002**, *12*, 653.

[10] D. V. Talapin, A. L. Rogach, A. Kornowski, M. Haase, H. Weller, *Nano Lett.* **2001**, *1*, 207.

[11] C. de Mello Donegá, S. G. Hickey, S. F. Wuister, D. Vanmaekelbergh, A. Meijerink, *J. Phys. Chem. B* **2003**, *107*, 489.

[12] a) Y. Zhou, H. Zhu, Z. Chen, M. Chen, Y. Xu, H. Zhang, D. Zhao, *Angew. Chem. Int. Ed.* **2001**, *40*, 2166. b) F. Gao, Q. Lu, S. Xie, D. Zhao, *Adv. Mater.* **2002**, *14*, 1537.

[13] a) T. Rajh, O. I. Miæiæ, A. J. Nozik, *J. Phys. Chem.* **1993**, *97*, 11 999. b) A. L. Rogach, L. Katsikas, A. Kornowski, D. Su, A. Eychmüller, H. Weller, *Ber. Bunsen-Ges.* **1996**, *100*, 1772.

[14] X. Peng, *Chem. Eur. J.* **2002**, *8*, 334.

[15] L. Qu, X. Peng, *J. Am. Chem. Soc.* **2002**, *124*, 2049.

[16] a) A. Schroedter, H. Weller, *Angew. Chem. Int. Ed.* **2002**, *41*, 3218. b) W. J. Parak, R. Boudreau, M. L. Gros, D. Gerion, D. Zanchet, C. M. Micheel, C. Williams, A. P. Alivisatos, C. Larabell, *Adv. Mater.* **2002**, *14*, 882.

Monodispersed ZnS Dimers, Trimers, and Tetramers for Lower Symmetry Photonic Crystal Lattices**

By *Chekesha M. Liddell** and *Christopher J. Summers*

The production of monodispersed non-spherical particles is necessary to fully explore the promise of colloidal systems for optical pigments[1] and for photonic crystal applications.[2–6] For example, pigments containing 3- and 4-"lobed" latex clusters exhibited high shear viscosity without the use of steric stabilization or rheology modifiers over a broad range of shearing conditions.[1] In the case of photonic crystals, the addition of asymmetry in the lattice is predicted to enable photonic bandgap realization at refractive index values that are insufficient for assemblies of monodispersed spheres.[7] Additionally, complex building blocks lower the filling fraction of high index material by the geometrical restrictions of their packing so that inverting the structures may not be required.[2,7]

Though numerous studies have been conducted on close packed assemblies of spherical particles, similar work employing non-spherical colloids is comparatively scarce. Several indirect techniques that form non-spherical particles from their spherical precursors, typically in small quantities, have proven successful. Snoeks, van Blaaderen, and their co-workers have used ion irradiation to anisotropically deform ZnS, SiO_2, TiO_2, Fe_2O_3, and ZnS(core)–SiO_2(shell) spheres into ellipsoids.[5,8,9] The transverse axis of the ellipsoids showed a linear increase with ion fluence, i.e., the aspect ratio could be continuously tuned by varying the irradiation fluence. Xia and coworkers used geometrical confinement and attractive capillary forces to self-assemble polygonal and polyhedral clusters of precisely controlled size, shape, and structure from polystyrene beads. The beads were physically trapped in cylindrical

[*] Dr. C. M. Liddell, Dr. C. J. Summers
School of Materials Science and Engineering
Georgia Institute of Technology
Atlanta, GA 30 332 (USA)
E-mail: gt2012a@prism.gatech.edu

[**] This work has been supported in part by the Army Research Office MURI program (DAAD19-01-1-0603). C. M. Liddell thanks the Office of Naval Research for fellowship support. The authors also thank J. Li and Z. L. Wang, Georgia Tech Electron Microscopy Center, for TEM imaging and helpful discussion and Jonafel Crowe, Petit Institute of Bioengineering and Biosciences, for aid in flow cytometry experiments.

 DOI: 10.1002/adma.200305283

ADVANCED MATERIALS

holes with dimensions that dictated the cluster shape formed.[3,4]

Here, we report the preparation of hierarchically structured ZnS dimers, trimers, tetramers, and tetrahedra, monodisperse in size and shape via a two-stage chemical precipitation from metal salt and thioacetamide sulfide ion precursor. This method generates large quantities of high-refractive-index particles transparent in the near-infrared (IR) and visible regions. The particle morphology and formation mechanism were studied using electron microscopy. The shape distributions of the mixed morphology suspensions were determined using stereology and flow cytometry and were compared to the Smoluchowski model of rapid coagulation to suggest the coagulation stage most appropriate for collecting dimer particles for lower symmetry photonic crystal lattices.

Figure 1 shows a scanning electron microscopy (SEM) image illustrating the well-defined cluster types formed via the coagulation of spheres during synthesis from homogeneous solution[10] at elevated temperature. The low polydispersity,

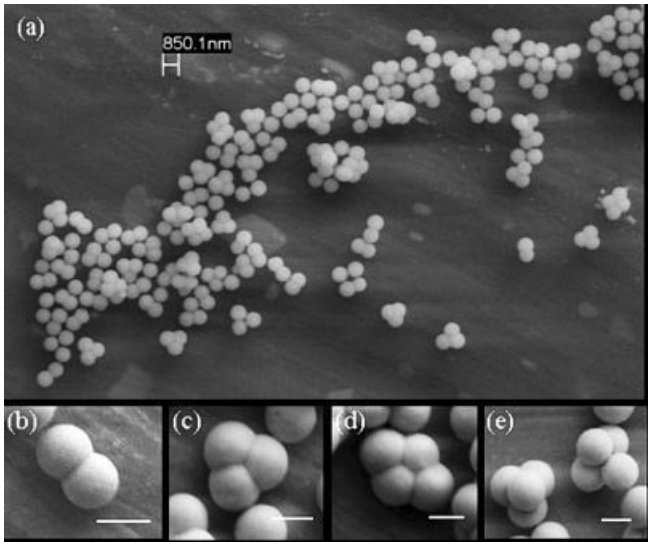

Fig. 1. SEM images of zinc sulfide colloidal clusters. a) Mixture of morphology classes deposited onto SEM stud from suspension; b) dimer; c) trimer; d) tetramer; e) tetrahedra. For (b–e) scale bars represent 880 nm, 800 nm, 640 nm, and 563 nm, respectively.

4.74 % for spheres and 5.67 % in the case of dimers, was derived from measuring 150 particles in the SEM images. The particles exhibited simple geometries reflecting cubic close packing. By varying the precipitation time at 85 °C batches of monodispersed spheres ranging in size from ~ 500 nm to 3 μm were obtained and clustered into dimers, trimers, tetramers, and tetrahedrons ~ 900 nm to 5 μm in their longest dimension. Undesirable irregular aggregation of the colloids was avoided under optimized synthesis conditions. The uniformity of each morphology type, low polydispersity, and capability to produce small sizes are important for generating highly ordered photonic crystals for the near-IR and visible regions.

The particle substructure, including primary crystallite size, structure, and orientation, was characterized by transmission electron microscopy (TEM). Particles were ground with mortar and pestle and fragments were examined. Figure 2 shows the 5–10 nm irregularly shaped primary crystallites. That the particles were aggregates of nanocrystals is consistent with previous studies on monodispersed ZnS spheres.[11,12] High-

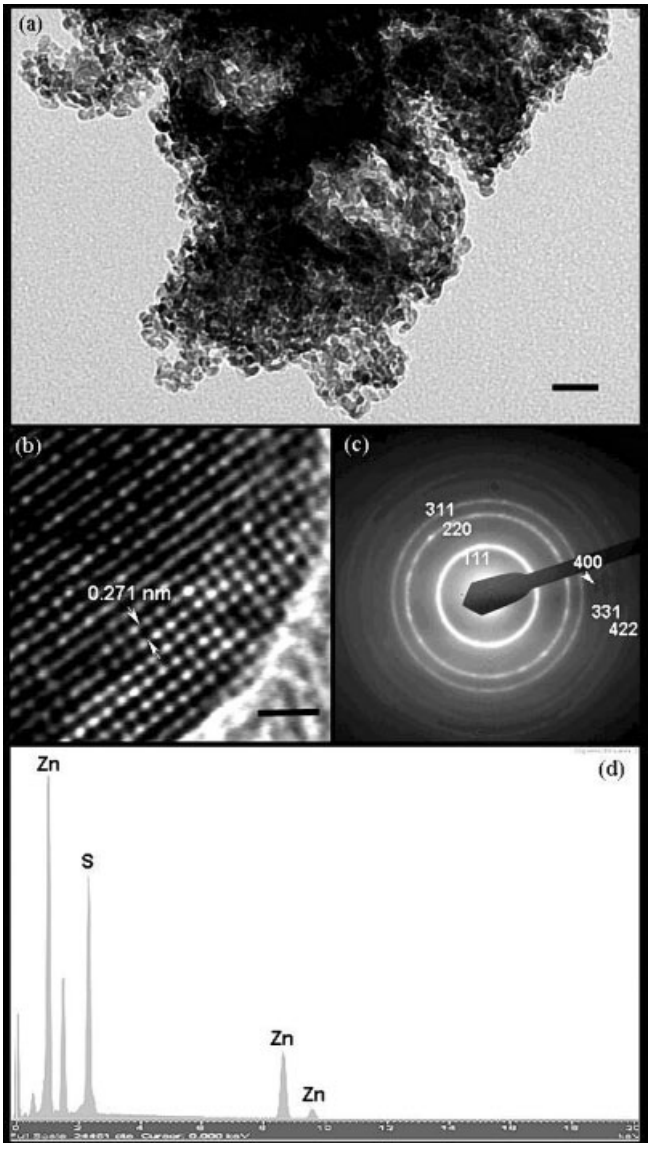

Fig. 2. Crystal structure and composition of ZnS colloidal clusters. a) TEM image indicating a particle substructure of ZnS nanocrystals 5–10 nm in size. Scale bar represents 30 nm. b) High-resolution TEM of a nanocrystallite showing its crystallinity and {200} interplanar spacing characteristic of the zinc blende structure. Scale bar represents 1 nm. c) Electron diffraction pattern recorded from the particles labeled with indices characteristic of the zinc blende structure. d) EDS spectrum of particles confirming the stoichiometric composition of zinc and sulfur (Al line at 1.4866 eV comes from the SEM stub).

resolution TEM confirmed that the crystalline phase was zinc blende. No amorphous material was detected. Measurements of the interplanar spacing of {200} planes on the [001] projected image matched the standard value for sphalerite ZnS, 0.2705 nm. The electron diffraction pattern shown in Figure 2c confirmed a long-range randomly oriented polycrystal-

line structure. The real space distance to the pattern center was measured and rings were indexed to six lines characteristic of sphalerite, {111}, {220}, {311}, {400}, {331}, and {422}. The {200}, {222}, and {420} reflections were quite weak or absent as expected from the arrangement of atoms in the zinc blende crystal structure. A 1:1 stoichiometric composition of zinc and sulfur was determined by energy dispersive X-ray spectroscopy (EDS).

Figure 3 shows the fracture surface along the dimer axis of rotation. The aspect ratio, i.e., dimer length to constituent sphere diameter, was 1.6 indicating the significant intergrowth of the constituent monodispersed spheres. The rough particle

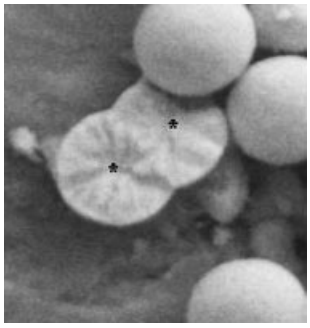

Fig. 3. Dimer fracture surface. Fracture surface features include a rough interface between constituent spheres and radial growth patterns originating from the center of the constituent spheres (locations marked with asterisks).

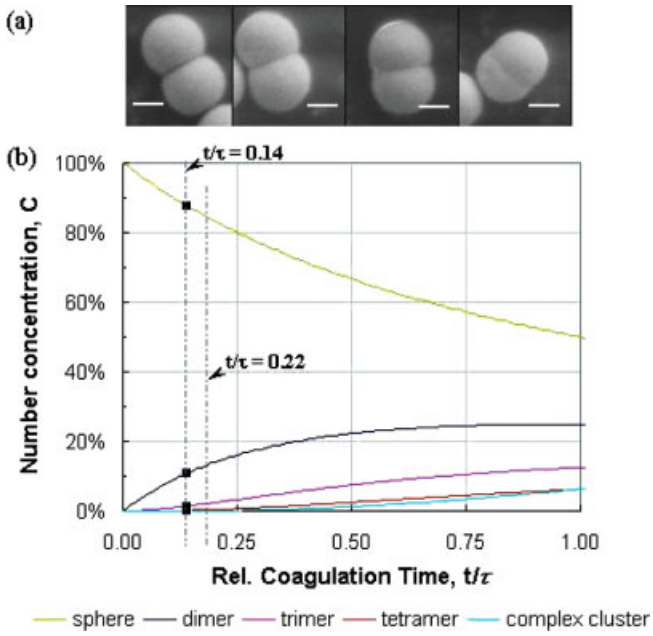

Fig. 4. Particle morphology development. a) Morphogenesis of dimer particle at different stages of coagulation. Particles from the same non-optimized synthesis batch showing polydispersity parallel to the dimer axis. b) Number percentage of spheres, dimers, trimers, tetramers, and complex clusters as a function of the relative coagulation time predicted by Smoluchowski's model of rapid flocculation. Complex clusters are taken as those having more than four constituent spheres. An experimental shape distribution from a batch of ZnS particles is indicated by the square data markers on the graphs.

interface observed on the fracture surface indicates primary crystallite rearrangement and fusion occurred at the sphere contacts. Isolated sphere surfaces appeared smooth in the SEM. The rearrangement and bonding of primary crystallites made aggregation irreversible, and spheres could not be separated once incorporated into a cluster without fracturing through solid material.

Examination of the fracture surface also indicated that secondary particle clustering occurred once the particles had reached ~97–100 % of the final size of the unclustered spheres, as measured from the diameter of constituent spheres compared to the average isolated sphere diameter. The dimer fracture surface exhibited two radial growth patterns initiating from well-separated seeds. If coagulation occurred very early in the growth stage, i.e., particles less than 100 nm, the fracture surface would be expected to show two asymmetric radial growth patterns originating from points closer to the interface. Faster growth along the radial directions, unhindered by the contact, would lead to seed sites less centrally located in the constituent spheres of the dimer. On a microscale, a size distribution in the direction perpendicular to the dimer axis might be expected. Instead, the size was uniform in the direction perpendicular to the dimer axis and the distribution in size occurred parallel to the axis. Figure 4a demonstrates the dimer size and shape differences in a non-optimized synthesis batch. That the dimer sizes are distributed primarily along the rotational axis supports a mechanism of coagulation of large secondary spherical particles. Such systems have been modeled by Smoluchowski's formulation for the rapid coagulation of monodispersed spheres.[13,14]

The Smoluchowski model considers only binary collisions where each collision results in permanent contact between particles. This only strictly holds in dilute solutions close to the isoelectric point of the particles where no interparticle forces are operative. The model does not consider coagulation during sphere growth or under conditions of continuous sphere nucleation as expected in this work, but in the absence of a more comprehensive model can be used to provide a qualitative understanding for the development of mixed cluster populations by the coagulation of monodispersed spheres. The number concentrations for each morphology type are plotted in Figure 4b. The figure shows that the dimer population reaches a maximum at $t/\tau = 1$, when the original number concentration of monodispersed spheres has been reduced by one half due to coagulation. However, this is not the optimum condition, at which to harvest dimers because as Figure 4b indicates there are also quite significant populations of trimers, tetramers, and complex clusters. To more easily obtain dimers, separation should be performed on samples at earlier stages in the coagulation i.e., $t/\tau < 0.22$, where morphology types having more than two constituent spheres are less than 2.5 % by number. In order to compare the degree of coagulation of the ZnS colloids with the theoretical distributions, it was necessary to quantify the population distributions.

The volume percentage of each morphological type was estimated using a point counting stereology technique as will be

ADVANCED MATERIALS

described in detail elsewhere. Stereological analysis of SEM images allows the accurate estimation of three-dimensional structural parameters and their standard deviations from two-dimensional projections.[15] Flow cytometry was also employed as an independent instrumental method and results were compared to findings using stereology. Siiman et al. used the flow cytometry light scattering characteristics, i.e., side scatter versus intermediate angle (10–20°) or (20–65°) scattering to determine the relative populations of singlets, doublets, and higher order multiplets, in suspensions of gold- and silver-coated polystyrene beads ~2 μm in size.[16] In the present work, ZnS particles were analyzed with a Beckton Dickson FACS Vantage flow cytometer in a streaming flow of 0.9 % sodium chloride aqueous solution. The forward scatter versus side scatter dot plot obtained is provided in Figure 5.

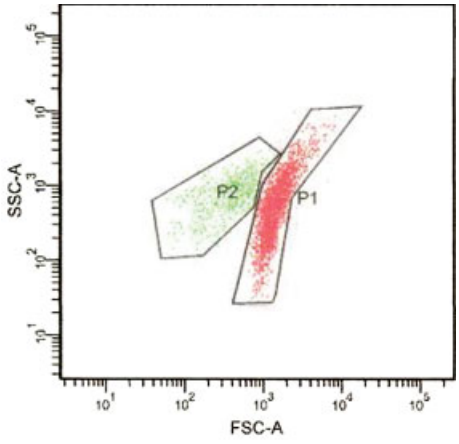

Fig. 5. Flow cytometry forward scatter (FSC) vs. side scatter (SSC) dot plot of sphere-dimer mixed suspension showing separable light scattering characteristics for the two populations.

The sphere and dimer populations were differentiable by their forward and side light-scattering characteristics. From the gating strategy shown, the relative amounts of spheres (P1) and dimers (P2) were 81.7 vol.-% and 18.3 vol.-%, respectively. The percentages were calculated from the number of light scattering events detected from the interaction of the incident beam with the particles. The percentages agreed, within the error range, with those determined using the stereological method, 78.53 ± 3.77 % spheres and 19.98 ± 2.73 % dimers. The corresponding t/τ value was obtained by converting volume percent to number percent (88 no.-% spheres, 11 no.-% dimers) and comparing to the Smoluchowski model as shown in Figure 4. The experimental data matched the theoretical distribution corresponding to a t/τ value of 0.13–0.14, which is in the region of easily separable mixtures. In addition, quantities of dimers up to 23 vol.-% were obtained under optimal synthesis conditions. This corresponded to ~10^{12} dimers, several orders of magnitude greater than indirect non-spherical particle synthesis methods,[4] which produced ~10^5 dimers. Isolated dimer populations can be used in directed assembly studies of non-spherical colloids to achieve lower symmetry photonic crystal structures such as the diamond-analog proposed by Li, Wang, and Gu.[7]

In summary, monodispersed ZnS clusters of close-packed shapes including dimers, trimers, and tetrahedra have been synthesized. The non-spherical particles are hierarchically structured, composed of 500 nm–3 μm coagulated monodispersed spheres, which are themselves aggregates of 5–15 nm irregular single crystal spheroids. The mixtures of morphological types were quantitatively analyzed by image analysis and stereology, as well as flow cytometry. Dimers were obtained in large quantities for harvesting and use in photonic crystal applications. Though the production of monodispersed ZnS spheres by the decomposition of thioacetamide in the presence of zinc salts has been utilized by several groups,[8–12] to our knowledge, this is the first report of their controlled coagulation leading to separable quantities of well-defined non-spherical ZnS colloids. These high-refractive-index particles (relative to silica and polystyrene) expand the menu of complex colloid bases available for photonic crystal structures and can be used in studies considering the effects of building block orientation on photonic band structures. Additionally, relatively small percentages, less than 5 vol.-%, can be added as dopants to sphere lattices for the engineering of optical microcavity effects.

Experimental

The ZnS colloidal clusters were precipitated via a two stage process from aqueous solutions with fixed composition 0.024 M Zn^{2+}, 0.00048 M Mn^{2+}, and 0.143 M thioacetamide (TAA). TAA was added to the mixed cation solutions at room temperature. The solutions were acidified with 0.800 ± 0.001 mL of 15.8 M HNO_3. The reactions were carried out in 200 mL Erlenmeyer flasks sealed with laboratory film. The reaction vessels were immersed in a constant temperature water bath for 4–6 h at 26–32 °C. The solutions were then placed in a second bath at 85 °C to grow colloidal clusters. The reactions were terminated after 20–35 min by quenching the solutions to below 10 °C in an ice bath. ZnS particles were separated from the mother liquid by centrifugation and were redispersed and washed three times with ultrapure water. The particles were collected by filtration on 0.22 μm cellulose ester membranes.

In preparation for TEM imaging, particles were ground with mortar and pestle in ethanol. The particle fragments were deposited from suspension onto 200-mesh nickel grids with carbon stabilized formvar support film. The fragments were examined using a JEOL 4000EX high-resolution TEM at an operating voltage of 400 kV. SEM images of uncoated particles were obtained in an LEO 1530 thermally-assisted field emission gun, SEM at 5 kV. The average size, standard deviation, and coefficient of variation were derived from SEM images, typically by measuring 100 spheres and 50 dimers. The diameter of spheres and longest dimension of dimers were measured. EDS was performed during SEM measurements at 20 kV on the INCA EDS detector manufactured by Oxford Instruments, Concord, MA.

For stereology analysis, SEM images were overlaid with a grid of 728 evenly spaced test points. The number of test points falling on a particular morphological type were counted and divided by the total number of test points falling on particles, regardless of their morphology. This point fraction was determined for each morphological type. The volume fraction of each particle species was estimated by averaging the point fraction over 10 microstructural fields.

Flow cytometry was performed on ZnS particle suspensions with the FACS Vantage SE Flow cytometer. The particles were analyzed with 488 nm Ar ion laser excitation in a streaming flow of 0.09 % NaCl aqueous solution.

Received: April 18, 2003
Final version: July 14, 2003

[1] C.-S. Chou, A. Kowalski, J. M. Rokowski, E. J. Schaller, *J. Coat. Technol.* **1987**, *59*, 93.
[2] Y. Lu, Y. Yin, Y. Xia, *Adv. Mater.* **2000**, *12*, 415.
[3] Y. Yin, Y. Xia, *Adv. Mater.* **2001**, *13*, 267.
[4] Y. Yin, Y. Lu, Y. Xia, *J. Am. Chem. Soc.* **2001**, *123*, 771.
[5] E. Snoeks, A. van Blaaderen, T. van Dillen, C. M. van Kats, K. Velikov, M. L. Brogersma, A. Polman, *Adv. Mater.* **2001**, *12*, 1511.
[6] P. Jiang, J. F. Bertone, V. L. Colvin, *Science* **2001**, *291*, 453.
[7] Z. Li, J. Wang, B. Gu, *J. Phys. Soc. Jpn.* **1998**, *67*, 3288.
[8] E. Snoeks, A. van Blaaderen, T. van Dillen, C. M. van Kats, K. Velikov, M. L. Brogersma, A. Polman, *Nucl. Instrum. Methods Phys. Res., Sect. B.* **2001**, *178*, 62.
[9] K. P. Velikov, A. van Blaaderen, *Langmuir* **2001**, *17*, 4779.
[10] D. M. Wilhelmy, E. Matijevic, *J. Chem. Soc. Faraday Trans.* **1984**, *80*, 563.
[11] Y. Tian, A. D. Dinsmore, S. B. Qadri, B. R. Ratna, *Mater. Res. Soc. Symp. Proc.* **1999**, *536*, 205.
[12] S. M. Scholz, R. Vacassy, L. Lemaire, J. Dutta, H. Hofmann, *Appl. Organomet. Chem.* **1998**, *12*, 327.
[13] A. E. Nielsen, *Kinetics of Precipitation*, Pergamon Press Ltd, New York **1964**, Ch. 9.
[14] W. Stober, A. Berner, R. Blaschke, *J. Colloid Interface Sci.* **1969**, *29*, 710.
[15] A. M. Gokhale, W. J. Drury, B. Whited, *Mater. Charact.* **1993**, *31*, 11.
[16] O. Siiman, K. Gordon, A. Burshteyn, J. A. Maples, J. K. Whitesell, *Cytometry* **2000**, *41*, 298.

Ferromagnetic Spots in Graphite Produced by Proton Irradiation**

By *Kyoo-hyun Han*, *Daniel Spemann*, *Pablo Esquinazi*,* *Roland Höhne*, *Volker Riede*, and *Tilman Butz*

Due to the fine-tuning possibilities of the building blocks and demands for environmental protection, organic molecular magnetic materials composed only of light elements (C,H,N,O,S) are considered potential candidates for magnetic applications. However, for these applications it is necessary that the magnetic state (ferromagnetism or ferrimagnetism) is stable at room temperature. This was believed to be only possible in materials containing metallic 3-d or 4-f elements. As a matter of fact, recording media are in general polycrystalline, granular or amorphous ferromagnetic metals, alloys and oxides. Recent reports, however, showed weak ferromagnetic signals at room temperature and above in highly oriented pyrolytic graphite[1] (HOPG) and in polymerized fullerene.[2,3] Nevertheless, magnetism experts are highly skeptical about room-temperature ferromagnetism in carbon-based materials without magnetic ions. Recently, unusually large ferromagnetic signals were found in meteoritic graphite.[4] This large ferromagnetic signal was interpreted as induced by magnetite (Fe_3O_4) inclusions in the graphite structure by a magnetic proximity effect.[4] It is interesting to note that in spite of some reports in the past—casting doubts on simple interpretations of ferromagnetism in carbon-based materials in terms of ferromagnetic impurities[5]—it appears that prejudices against a possible intrinsic origin of the observed ferromagnetism hindered a broad and rush development of these organic ferromagnets. In this work, we produced localized ferro- or ferrimagnetic spots (a few micrometers in diameter) on clean HOPG surfaces using a proton microbeam. Our results rule out the influence of ferromagnetic impurities and open up a new field of investigation with clear implications for future applications of metal-free carbon ferromagnets.

Clean surfaces of a HOPG sample (Advanced Ceramic, Fe content < 0.3 ppm, rocking-curve width= 0.4°) were irradiated by 2.25 MeV protons using a microbeam applied parallel to the *c*-axis. Beam diameters between 1 and 2 μm, separated by 20 μm, and at different fluences and doses were chosen. The total deposited electric charge (areal) density was between 0.05 and 50 nC μm^{-2}. The irradiated areas and surroundings were characterized simultaneously by atomic force (AFM) and magnetic force microscopy (MFM) at room temperature, operating in the "Tapping/Lift" scanning mode, using Si cantilevers with pyramidal tips coated with a magnetic CoCr film alloy magnetized perpendicular to the sample surface. Micro-Raman characterization of the spot areas was used to determine the degree of disorder.

Figure 1a shows the MFM images and Figure 1b the line scans of the topography and MFM signals obtained in three areas of the HOPG sample before irradiation. For virgin graphite samples, even though the changes in topography are significant, one obtains in general a MFM signal with a phase shift of the order of ±0.1°, which corresponds to the noise of

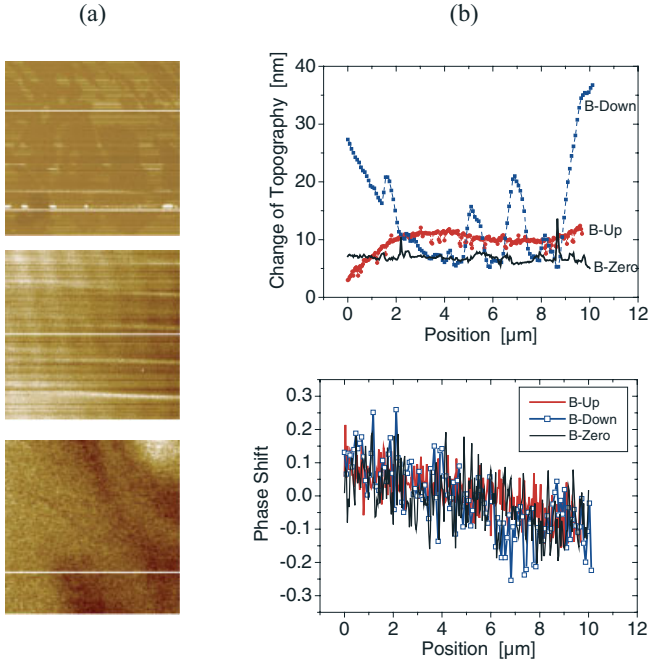

Fig. 1. a) Magnetic force gradient images (10 × 10 μm^2) of three unirradiated areas of graphite. The images were taken, from top to bottom, before field application, after applying a field of ~0.1 T in the +*z* direction (normal to the surface, parallel to the *c*-axis, *B*-up), and in the –*z* direction (*B*-Down). The tip-to-sample distance was 50 nm. b) The corresponding height (top) and phase shift (bottom) obtained at the line scans (white lines in (a)).

[*] Prof. P. Esquinazi, Dr. K.-h. Han, D. Spemann, Dr. R. Höhne, Dr. V. Riede, Prof. T. Butz
Institut für Experimentelle Physik II
Universität Leipzig
Linnéstrasse 5, D-04103 Leipzig (Germany)
E-mail: esquin@physik.uni-leipzig.de

[**] This work is supported by the Deutsche Forschungsgemeinschaft under DFG ES 86/6-3.

 DOI: 10.1002/adma.200305194